Measurement report: Formation and brownness of aqueous secondary organic aerosol from the aged biomass-burning emissions in the Sichuan Basin, China

Chao Peng[1,2,3,4], Yan Ding[4], Zhenliang Li[1,2,3], Tianyu Zhai[4], Xinping Yang[4], Mi Tian[6], Yang Chen[5], Xin Long[5], Haohui Tang[6], Guangming Shi[7], Liuyi Zhang[8], Kangyin Zhang[8], Fumo Yang[7], and Chongzhi Zhai[1,2,3]

[1]Chongqing Academy of Ecology and Environmental Sciences, Chongqing, 401336, China

[2]Chongqing Branch Academy of Chinese Research Academy of Environmental Sciences, Chongqing, 401336, China

[3]Chongqing Key Laboratory of Urban Atmospheric Environment Observation and Pollution Prevention, Chongqing, 401336, China

[4]Chinese Research Academy of Environmental Sciences, Beijing 100012, China

[5]Chongqing Institute of Green and Intelligent Technology, Chinese Academy of Sciences, Chongqing, 400714, China

[6]College of Environment and Ecology, Chongqing University, Chongqing, 400045, China

[7]College of Carbon Neutrality Future Technology, Sichuan University, Chengdu, 610065, China

[8]Chongqing Three Gorges University, Wanzhou, 404000, China

Correspondence: Chao Peng (pengchao0623@sina.com) and Chongzhi Zhai (czz66818@sina.com).

Number of pages: 18

Number of Texts: 3

Number of Figures: 10

Text S1. Source Apportionment of OA

Here, the positive matrix factorization (PMF) and multilinear engine (ME2) were implemented on the OA data measured by ToF-ACSM to determine the numbers and types of OA source factors (Paatero 1999; Paatero and Tapper 1994). The optimal number was selected by the discrimination of the tracers and the spectrum pattern of each source. Hydrocarbon-like OA (HOA) was dominated by alkyl ions with prominent ion fragments at $C_nH^+_{2n-1}$ and $C_nH^+_{2n+1}$ (m/z 41, 43, 55, 57, 69, 71, 83, and 85) in the spectra (Elser et al., 2016). Biomass-burning OA (BBOA) was identified by significant contributions from m/z 60 ($C_2H_4O_2^+$) and m/z 73 ($C_3H_5O_2^+$), they were the fragments of levoglucosan and mannosan emitted from incomplete biomass burning (Alfarra et al., 2007). Coal-combustion OA (CCOA) was characterized by unsaturated hydrocarbon ion fragments such as PAH-related ion fragments (i.e., m/z 77, 91, 115) (Sun et al., 2016). Oxygenated OA (OOA) was distinguished by the prominent signal of m/z 43 ($C_2H_3O^+$) and m/z 44 (CO_2^+) (Ng et al., 2011). Aqueous-phase oxidized OA (aqSOA) also had high correlation with m/z 43 and m/z 44, while it might show a significantly higher m/z 29 (CHO^+) signal than other OA factors (Zhao et al., 2019; Zhong et al., 2021).

We performed the free PMF runs from 3 to 6 factors. Q/Qexp result showed that N = 5 could be a reasonable result. Though BBOA and CCOA were separated, there was still a mix among POA factors, such as cooking-related OA (COA) might mix with HOA. Therefore, we tried to constrain COA by using different COA profiles in ME-2 to identify if COA factor could be resolved from the OA sources. HOA was constrained by using the profile from Ng et al. (2011), and COA was tried to constrain by Elser et al. (2016). However, a large amount of blank values were shown, indicating COA was absent during the campaign. Here, BBOA and CCOA were constrained by using the

BBOA profile of Zhong et al. (2020) and CCOA profile of Wang et al. (2017), respectively.

The restriction method ME2 was used to minimize PMF rotational ambiguity by the *a*-values from 0 to 1 with a step of 0.1 based on the reasonable result of PMF solutions, when HOA and CCOA were freely combined by 11 *a* value variables. The signal of m/z 60 was minimized in HOA, and the average fractional contribution of m/z 60 during the campaign (0.0103) was the maximal threshold to minimize the mix of BBOA from HOA. When the *a*-values were set from 0 to 1, the HOA fractional contribution was varied from 0.0067 to 0.0189, therefore the HOA solutions with *a*-values from 0.7 to 1 were deleted. Moreover, the CCOA solutions with *a*-values from 0.7 to 1 also be eliminated based on the estimating optimal *a*-values method. Overall, 20 PMF solutions were retained and the average value was the final result as shown in Fig. S3.

Text S2. Estimation of Primary and Secondary BrC Absorption

Aerosol light absorption (Abs_{λ}) is caused by BC ($Abs_{\lambda,BC}$), primary BrC ($Abs_{\lambda,BrC,pri}$), and secondary BrC ($Abs_{\lambda,BrC,sec}$). The $Abs_{\lambda,BrC,sec}$ value was estimated by a minimum R-squared (MRS) method at each wavelength developed from the BC-tracer method (Wang et al., 2019; Wu et al., 2016):

$$Abs_{\lambda,BrC}=Abs_{\lambda,BrC,pri}+Abs_{\lambda,BrC,sec} \quad \text{(S1)}$$

$$Abs_{\lambda,BrC,sec}=Abs_{\lambda,BrC}-\left(\frac{Abs_{\lambda,BrC}}{BC}\right)_{pri}\times BC \quad \text{(S2)}$$

where BC is the mass concentration ($\mu g\ m^{-3}$); $(Abs_{\lambda,BrC}/BC)_{pri}$ is the ratio of $Abs_{\lambda,BrC}$ to BC mass concentration in primary emissions ($m^{-2}\ g^{-1}$). The BC mass concentration and $Abs_{\lambda,BrC,sec}$ values caused by SOA were independent (Shrivastava et al., 2017).

Here, a series of arbitrary values for $(Abs_{\lambda,BrC}/BC)_{pri}$ from 0 to 40 in increments of 0.01 was used to calculate a set of $Abs_{\lambda,BrC,sec}$ values at each wavelength. A coefficient of determination (R^2) for the relationship between $Abs_{\lambda,BrC,sec}$ and BC mass concentration was derived. Detailed information on the method and validation of this approach could be found in Wu et al. (2024). Fig. S5 showed the series of R^2 values plotted against the assumed values of $(Abs_{\lambda,BrC}/BC)_{pri}$. As BC and $Abs_{BrC,sec,\lambda}$ were independent, the target value of $(Abs_{\lambda,BrC}/BC)_{pri}$ corresponded with the minimum R^2 ($Abs_{\lambda,BrC,sec}$, BC) was chosen to analyse at each wavelength. The bias of MRS result was < 23% when the measurement uncertainty was within 20% (Wu et al., 2016). The negative estimated $Abs_{BrC,sec,\lambda}$ values were set to zero, and the corresponding $Abs_{BrC,pri,\lambda}$ was taken as the observed $Abs_{BrC,\lambda}$.

Text S3. Assessment of a Multiple Linear Regression Method

In this study, the estimate of $Abs_{\lambda,BrC}$ for each OA component, obtained through the multiple linear regression (MLR) method reconstruction, was evaluated by the normalized mean bias (NMB), root mean square error (RMSE), and index of agreement (IOA). These parameters were calculated as follows (Li et al., 2011):

$$\mathrm{NMB}=\frac{\sum_{i=1}^{N}(P_i-O_i)}{\sum_{i=1}^{N}O_i} \tag{S5}$$

$$\mathrm{RMSE}=\left[\frac{1}{N}\sum_{i=1}^{N}(C)^2\right]^{\frac{1}{2}} \tag{S6}$$

$$\mathrm{IOA}=1-\frac{\sum_{i=1}^{N}(P_i-O_i)^2}{\sum_{i=1}^{N}(|P_i-\bar{O}|+|O_i-\bar{O}|)^2} \tag{S7}$$

where P_i and O_i were the $Abs_{\lambda,BrC}$ estimated by MLR method and measured by AE33, respectively; N was the total number of predictions used for comparison; $\bar{O}$ denoted the average of the observed $Abs_{\lambda,BrC}$. The IOA ranged from 0 to 1, with 1 indicating perfect agreement of $Abs_{\lambda,BrC}$ between the MLR reconstruction and AE33 measurement.

During the campaign, the NMB values of $Abs_{\lambda,BrC}$ were 11.8%, 32.0%, 26.6%, 25.3%, and 13.3% at 370, 470, 520, 590, and 660 nm, respectively. Meanwhile, the RMSE values of $Abs_{\lambda,BrC}$ were 13.5, 7.5, 4.7, 3.1, and 1.7 Mm^{-1}, respectively. The IOA values at each wavelength (0.99–1.00) were higher than 0.95. Additionally, as shown in Fig. S7, the $Abs_{\lambda,BrC}$ values estimated by MLR method showed the best correlations (r^2 = 0.86, 0.84, 0.78, 0.61, 0.54, respectively, $p < 0.001$) with those measured by AE33 at 370, 470, 520, 590, and 660 nm, respectively. The slopes of these relationships between $Abs_{\lambda,BrC}$ measured by AE33 and estimated by MLR method were 0.81, 0.96, 0.78, 0.61, and 0.54, respectively.

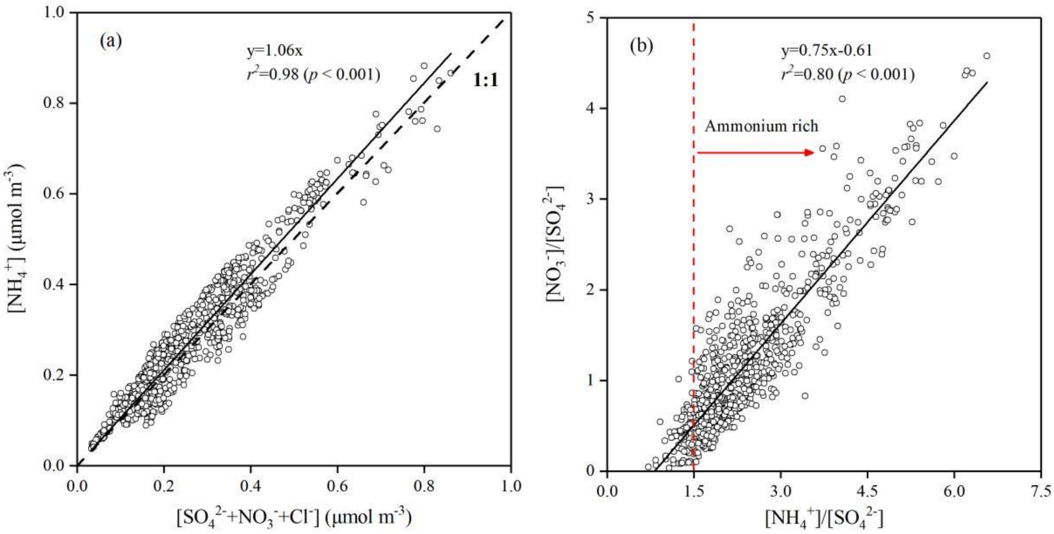

Figure S1. Scatter plots of **(a)** molar concentrations of NH_4^+ versus the sum of SO_4^{2-}, NO_3^-, and Cl^-, **(b)** molar ratios of NO_3^- to SO_4^{2-} versus NH_4^+ to SO_4^{2-}.

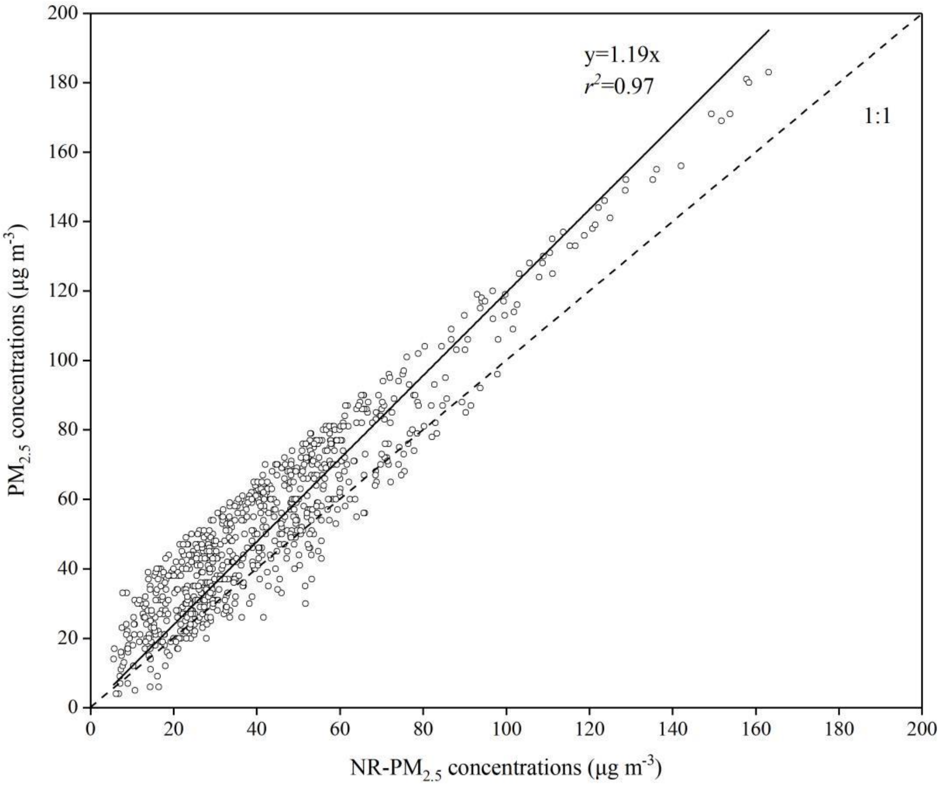

Figure S2. Scatter plot of $PM_{2.5}$ concentrations measured by a thermal analyzer (5030i) versus those measured by ToF-ACSM.

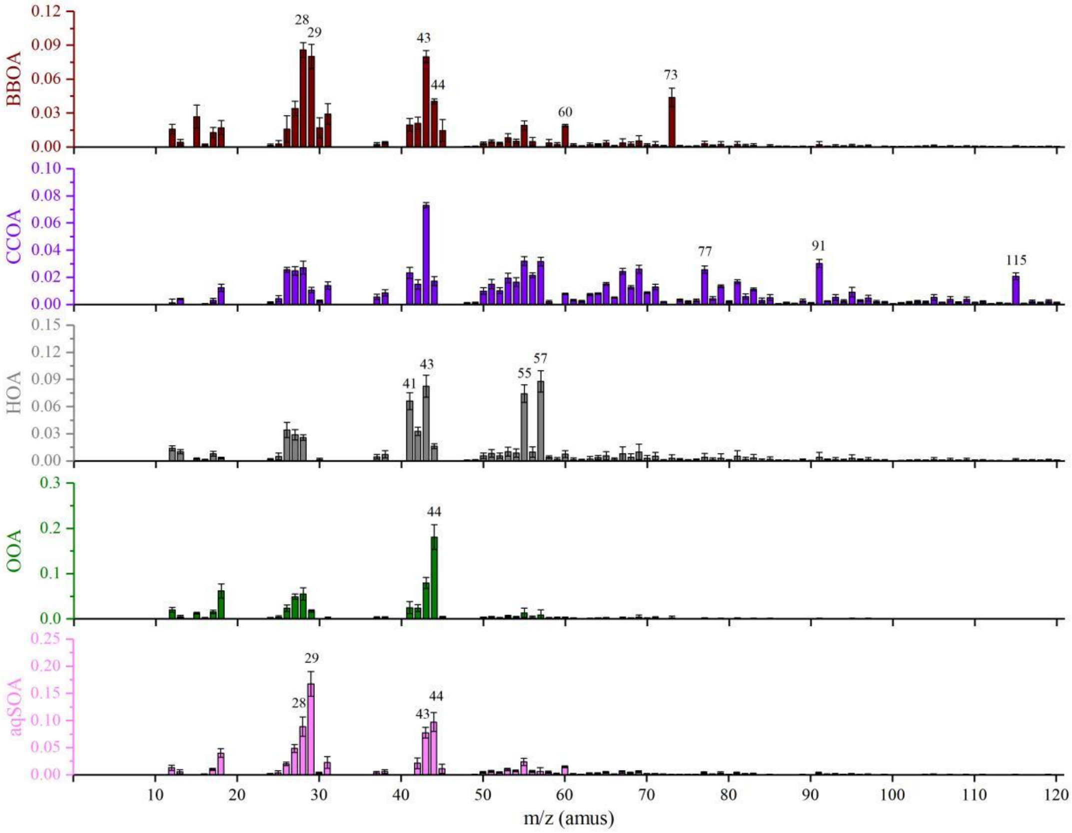

Figure S3. Mass spectra of six OA factors during the campaign.

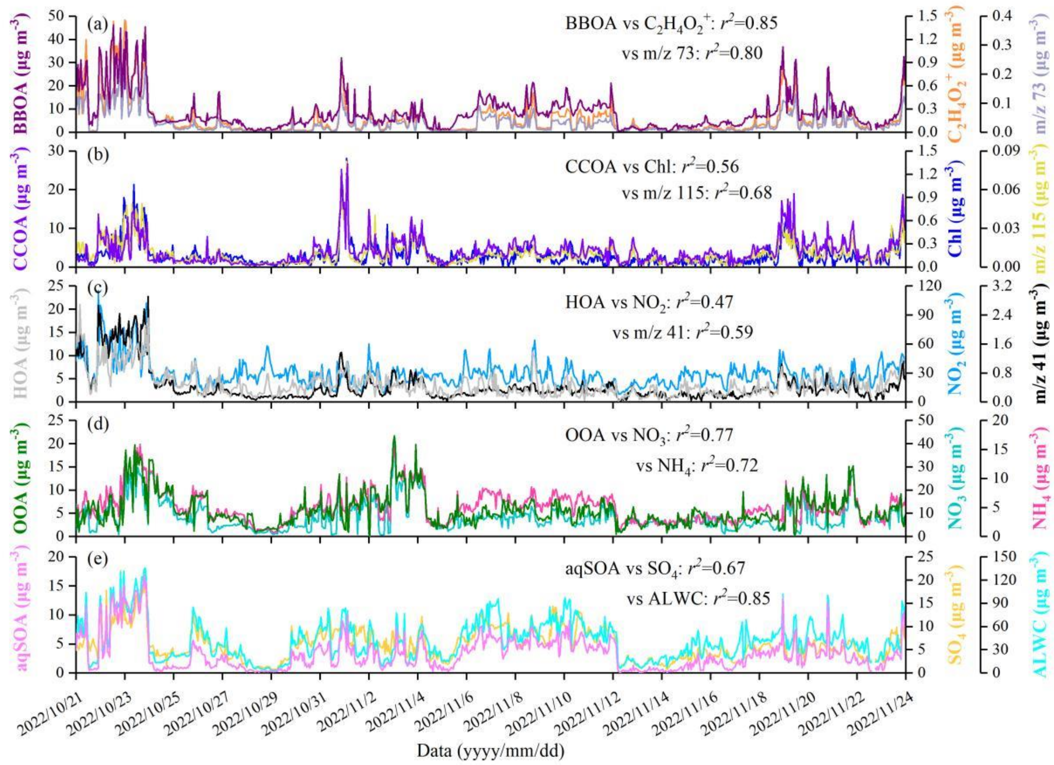

Figure S4. Time series of six OA factors and their corresponding tracer compounds.

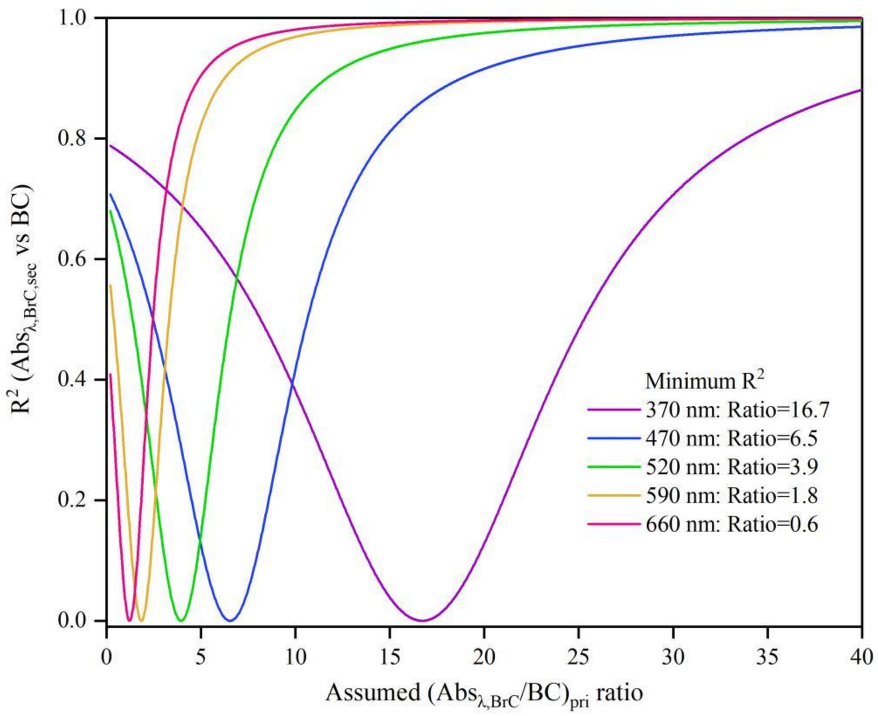

Figure S5. Coefficients of determination (R^2) for $Abs_{\lambda,BrC,sec}$ at 370, 470, 520, 590, and 660 nm versus BC mass concentrations plotted against the assumed ratios of $(Abs_{\lambda,BrC}/BC)_{pri}$.

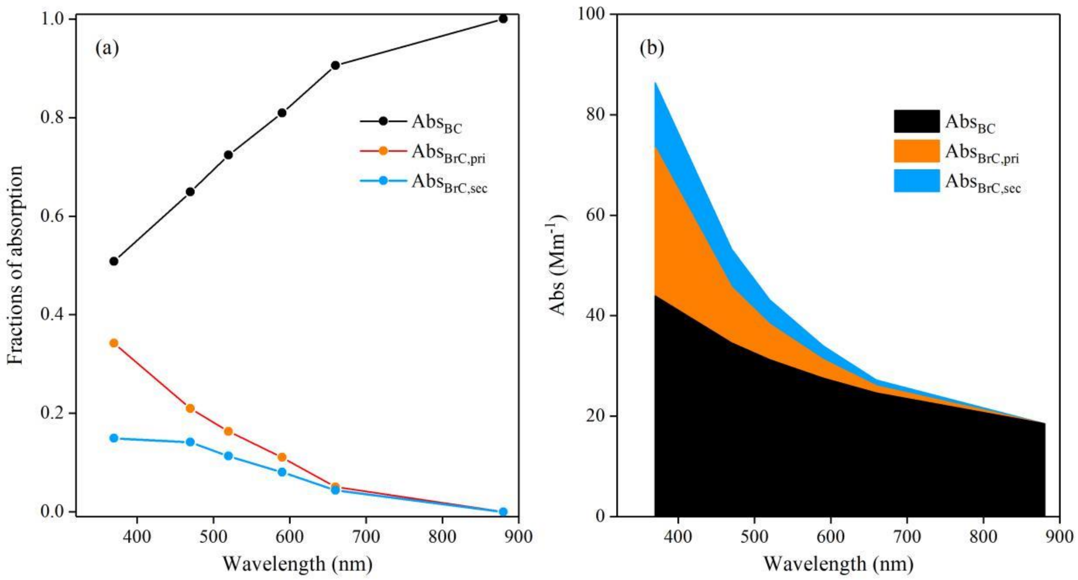

Figure S6. (a) Fractions and **(b)** contributions of Abs_{BC}, $Abs_{BrC,pri}$, and $Abs_{BrC,sec}$ to Abs at different wavelengths from 370 to 880 nm during the campaign.

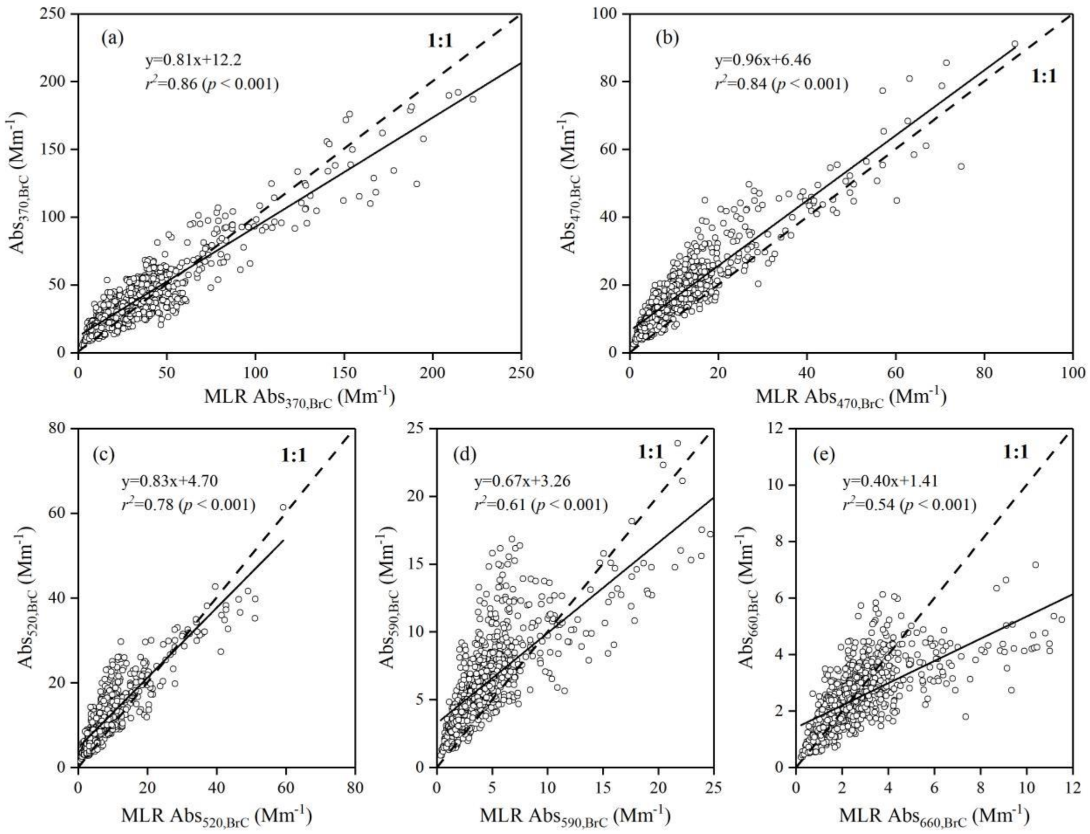

Figure S7. Scatter plots of $Abs_{370,BrC}$ at **(a)** 370, **(b)** 470, **(c)** 520, **(d)** 590, and **(e)** 660 nm measured by AE33 versus that obtained from a multiple linear regression (MLR) method.

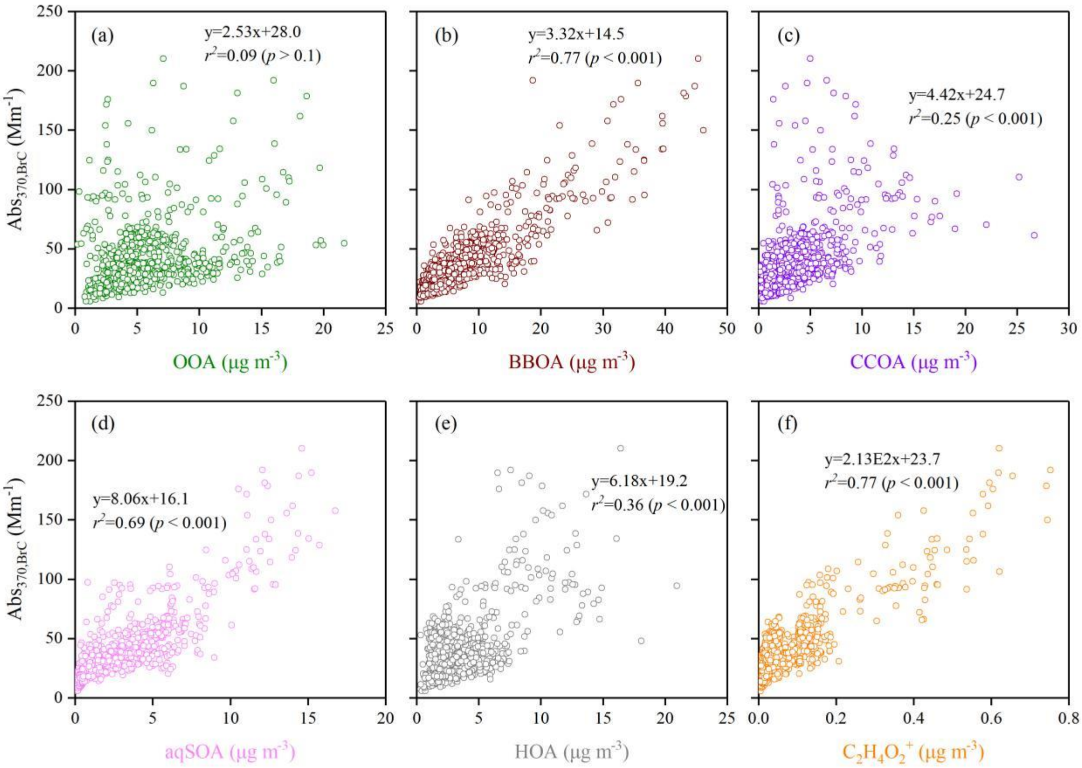

Figure S8. Correlation between $Abs_{370,BrC}$ and **(a)** OOA, **(b)** BBOA, **(c)** CCOA, **(d)** aqSOA, **(e)** HOA, and **(f)** $C_2H_4O_2^+$ mass concentrations.

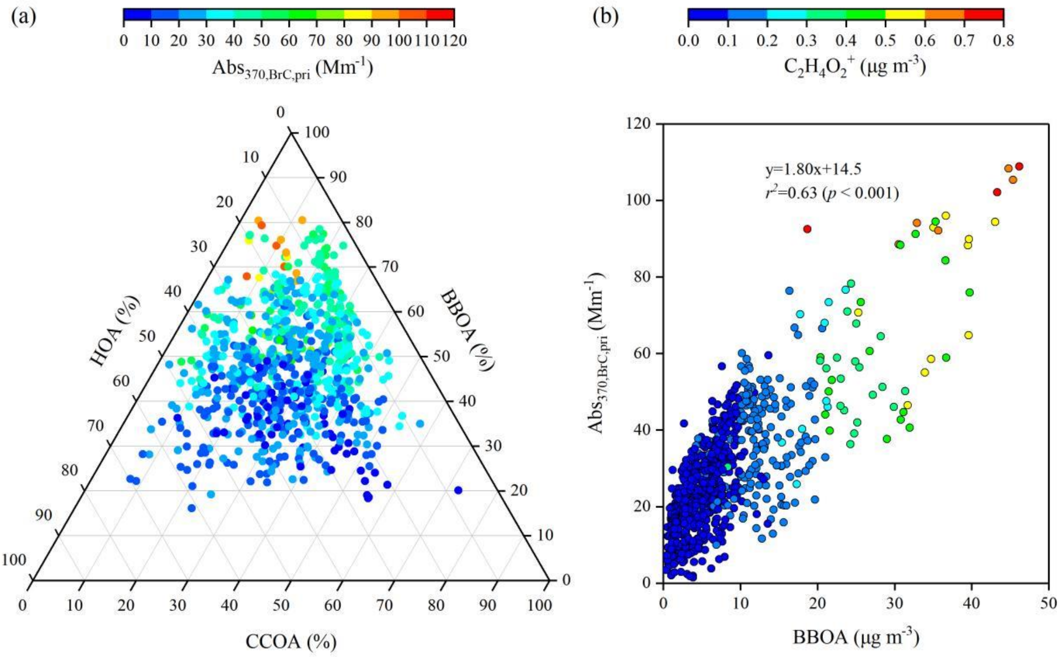

Figure S9. (a) Ternary diagram for the mass fractions of BBOA, CCOA, and HOA in POA colored by $Abs_{370,BrC,pri}$, and **(b)** scatter plot of BBOA mass concentrations versus $Abs_{370,BrC,pri}$ colored by $C_2H_4O_2^+$ mass concentrations.

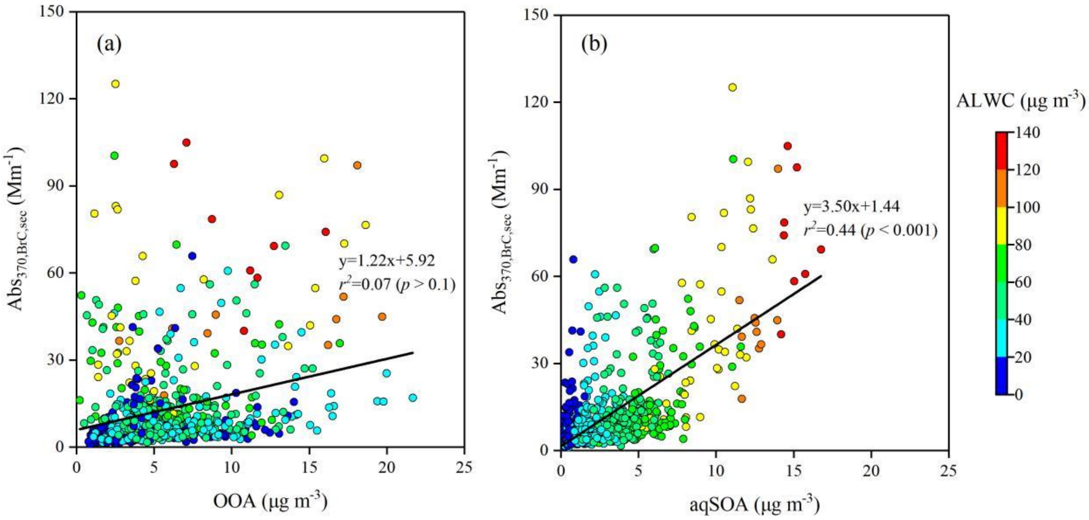

Figure S10. Scatter plots of $Abs_{370,BrC,sec}$ versus **(a)** OOA and **(b)** aqSOA mass concentrations colored by ALWC.

References

Alfarra, M. R., Prévôt, A. S. H., Szidat, S., Sandradewi, J., Sandradewi, S., Lanz, V. A., Schreiber, D., Mohr, M., and Baltensperger, U.: Identification of the Mass Spectral Signature of Organic Aerosols from Wood Burning Emissions, Environ. Sci. Technol., 41, 5770−5777, https://doi.org/10.1021/es062289b, 2007.

Elser, M., Huang, R. J., Wolf, R., Slowik, J. G., Wang, Q. Y., Canonaco, F., Li, G. H., Bozzetti, C., Daellenbach, K. R., Huang, Y., Zhang, R. J., Li, Z. Q., Cao, J. J., Baltensperger, U., El-Haddad, I., and Prévôt, A. S. H.: New insights into $PM_{2.5}$ chemical composition and sources in two major cities in China during extreme haze events using aerosol mass spectrometry, Atmos. Chem. Phys., 16, 3207−3225, https://doi.org/10.5194/acp-16-3207-2016, 2016.

Li, G., Bei, N., Tie, X., and Molina, L. T.: Aerosol effects on the photochemistry in Mexico City during MCMA-2006/MILAGRO campaign, Atmos. Chem. Phys., 11, 5169−5182, https://doi.org/10.5194/acp-11-5169-2011, 2011.

Ng, N. L., Canagaratna, M. R., Jimenez, J. L., Zhang, Q., Ulbrich, I. M., and Worsnop, D. R.: Real-Time Methods for Estimating Organic Component Mass Concentrations from Aerosol Mass Spectrometer Data, Environ. Sci. Technol., 45, 910−916, https://doi.org/10.1021/es102951k, 2011.

Paatero, P.: The Multilinear Engine: A Table-Driven, Least Squares Program for Solving Multilinear Problems, Including the n-Way Parallel Factor Analysis Model, J. Comput. Graph. Stat., 8, 854−888, https://doi.org/10.1080/10618600.1999.10474853, 1999.

Paatero, P. and Tapper, U.: Positive matrix factorization: A non-negative factor model with optimal utilization of error estimates of data values, Environmetrics, 5, 111−126, https://doi.org/10.1002/env.3170050203, 1994.

Shrivastava, M., Cappa, C. D., Fan, J., Goldstein, A. H., Guenther, A. B., Jimenez, J. L., Kuang, C., Laskin, A., Martin, S. T., Ng, N. L., Petaja, T., Pierce, J. R., Rasch, P. J., Roldin, P., Seinfeld, J. H., Shilling, J., Smith, J. N., Thornton, J. A., Volkamer, R., Wang, J., Worsnop, D. R., Zaveri, R. A., Zelenyuk, A., and Zhang, Q.: Recent advances in understanding secondary organic aerosol: Implications for global climate forcing, Rev. Geophys., 55, 509−559, https://doi.org/10.1002/2016RG000540, 2017.

Sun, Y. L., Du, W., Fu, P. Q., Wang, Q. Q., Li, J., Ge, X. L., Zhang, Q., Zhu, C. M., Ren, L. J., Xu, W. Q., Zhao, J., Han, T. T., Worsnop, D. R., and Wang, Z. F.: Primary and secondary aerosols in Beijing in winter: sources, variations and processes, Atmos. Chem. Phys., 16, 8309−8329, https://doi.org/10.5194/acp-16-8309-2016, 2016.

Wang, Q. Y., Ye, J. H., Wang, Y. C., Zhang, T., Ran, W. K., Wu, Y. F., Tian, J., Li, L., Zhou, Y. Q., Ho, H. S. S., Dang, B., Zhang, Q., Zhang, R. J., Chen, Y., Zhu, C. S., and Cao, J. J.: Wintertime Optical Properties of Primary and Secondary Brown Carbon at a Regional Site in the North China Plain, Environ. Sci. Technol., 53, 12389−12397, https://doi.org/10.1021/acs.est.9b03406, 2019.

Wang, Y. C., Huang, R. J., Ni, H. Y., Chen, Y., Wang, Q. Y., Li, G. H., Tie, X. X., Shen, Z. X., Huang, Y., Liu, S. X., Dong, W. M., Xue, P., Fröhlich, R., Canonaco, F., Elser, M., Daellenbach, K. R., Bozzetti, C., El Haddad, I., Prévôt, A. S. H., Canagaratna, M. R., Worsnop, D. R., and Cao, J. J.: Chemical composition, sources and secondary processes of aerosols in Baoji city of northwest China, Atmos. Environ., 158, 128−137, https://doi.org/10.1016/j.atmosenv.2017.03.026, 2017.

Wu, C. and Yu, J. Z.: Determination of primary combustion source organic carbon-to-elemental carbon (OC/EC) ratio using ambient OC and EC measurements: Secondary OC-EC correlation minimization method, Atmos. Chem. Phys., 16, 5453−5465, https://doi.org/10.5194/acp-16-5453-2016, 2016.

Wu, H., Peng, C., Zhai, T. Y., Deng, J. C., Lu, P. L., Li, Z. L., Chen, Y., Tian, M., Bao, Z. E., Long, X., Yang, F. M., and Zhai, C. Z.: Characteristics of light absorption and environmental effects of Brown carbon aerosol in Chongqing during summer and winter based on online measurement: Implications of secondary formation, Atmos. Environ., 338, 120843, https://doi.org/10.1016/j.atmosenv.2024.120843, 2024.

Zhao, J., Qiu, Y. M.,Zhou, W., Xu, W. Q., Wang, J. F., Zhang, Y. J., Li, L. J., Xie, C. H., Wang, Q. Q., Du, W., Worsnop, D. R., Canagaratna, M. R., Zhou, L. B., Ge, X. L., Fu, P. Q., Li, J., Wang, Z. F., Donahue, N. M., and Sun, Y. L.: Organic Aerosol Processing During Winter Severe Haze Episodes in Beijing, J. Geophys. Res.: Atmos., 124, 10248−10263, https://doi.org/10.1029/2019JD030832, 2019.

Zhong, H. B., Huang, R. J., Chang, Y. H., Duan, J., Lin, C. S., and Chen, Y.: Enhanced formation of secondary organic aerosol from photochemical oxidation during the COVID-19 lockdown in a background site in Northwest China, Sci. Total Environ., 778, 144947, https://doi.org/10.1016/j.scitotenv.2021.144947, 2021.

Zhong, H. B., Huang, R. J., Duan, J., Lin, C. S., Gu, Y. F., Wang, Y., Li, Y. J., Zheng, Y., Chen, Q., Chen, Y., Dai, W. T., Ni, H. Y., Chang, Y. H., Worsnop, D. R., Xu, W., Ovadnevaite, J., Ceburnis, D., and O'Dowd, C. D.: Seasonal variations in the sources of organic aerosol in Xi'an, Northwest China: the importance of biomass burning and secondary formation, Sci. Total Environ., 737, 139666, https://doi.org/10.1016/j.scitotenv.2020.139666, 2020.